The Effects of Surface Mechanical Attrition Treatment (SMAT) on the Electrochemical and Surface Properties of Alloy 600.

M. Faichuk[1], S. Ramamurthy[2] and W. M. Lau[1]
[1] University of Western Ontario, Ontario, Canada

Abstract

Alloy 600 steam generator (SG) tubing has been shown to be highly susceptible to stress corrosion cracking (SCC). Alloy 800 was developed as a replacement, though it has shown susceptibility to corrosion under certain conditions. Hence, surface mechanical attrition treatment (SMAT) was employed to alter the surface properties of the SG tubing with an objective of improving its corrosion resistance. Hardness and micro-strain measurements were performed to determine the changes in the physical properties. Modifications to the electrochemical and surface properties were investigated using electrochemical techniques, X-ray Photoelectron Spectroscopy (XPS) and Auger Electron Spectroscopy (AES).

1. Introduction

New materials are currently being studied for use in nuclear power stations as steam generator (SG) tubing. Alloy 600 used to be one of the "superalloys" for this application but numerous reports over the years have detailed the underlying issues with the Alloy 600 tubing, and the problem with its susceptibility to stress corrosion cracking (SCC) under normal operating conditions (1,2). The function of SG tubing in the CANDU™ reactors is to contain and separate the primary and secondary water sources as well as to transfer heat from the primary water to the secondary water. The operating conditions of the tubing are often quite harsh, having to withstand high pressures and temperatures. SCC is the result of a susceptible material exposed simultaneously to a corrosive environment and residual or applied stress, resulting in localized fracture. This type of corrosion can be very severe, as catastrophic damage can occur even though the stress levels are within the specified range (3). In the industrial setting, SCC of SG tubing in a CANDU™ reactor can result in highly radioactive primary water to leak out and mix with the secondary water. This creates enormous safety and financial problems, as the whole plant must be shut down in order to repair the tubing. A possible replacement for this material is Alloy 800, which was designed to be much more resistant to corrosion at higher temperatures (4). This type of tubing is already being used in reactors in Canada, Germany and other countries. Literature has shown that while Alloy 600 is much more susceptible to SCC, Alloy 800 itself is not totally immune. Recent reports have shown that under more extreme operating conditions, Alloy 800 has experienced SCC (5). SCC also becomes an issue when higher temperatures and pressures are used to maximize the efficiency of the CANDU™ reactors.

From these observations it is clear that a stronger, more corrosion resistant material is needed, being both durable and cost effective. A possible solution to this problem is to implement a cold working technique such as the surface mechanical attrition treatment

(SMAT) to change the surface properties of the SG tubing, including SCC. The SMAT was invented Professor Jian Lu and coworkers in late 90s and since then it has been used widely for producing nanostructured surface layer on bulk materials (6,7). In SMAT, smooth, spherical balls are placed into a vacuum sealed reflecting chamber and then driven into motion using a vibration generator. The sample material is impacted by these balls at random speeds and directions for a short period of time. The high strain and resulting temperature increases at the surface of the sample yields plastic deformation and grain refinement that can penetrate up to 50 μm. Under some conditions, a nanostructured layer can be formed (6,7).

Several Alloy 600 samples were treated using 2 mm diameter stainless steel balls with SMAT exposure for either 30, 90 or 120 minutes. A second set of samples were prepared using ZrO_2 balls for 15 and 30 minutes. The effects of the treatments were examined using microhardness testing and strain mapping. A series of electrochemical and surface analysis experiments were carried out on the treated samples. Polarization curves provided clues on the extent of corrosion resistance, while surface techniques such as X-ray photoelectron spectroscopy (XPS) and Auger electron spectroscopy (AES) provided composition and bonding information of the thin films formed.

2. Experimental

3/8” diameter Alloy 600 tubing specimens were procured from Rolled Alloys Canada in the mill-annealed condition. The composition of this alloy is presented in Table 1.

Element	Ni	Cr	Fe	Mn	Al	Ti	Si	Co
Composition %	Bal.	16.14	9.65	0.34	0.27	0.23	0.11	0.08

Table 1 Composition of Alloy 600 Tubing

Several sections of Alloy 600 tubing were subjected to SMAT. Process parameters were varied, such as the nature of the shots (stainless steel vs. ZrO_2) and the treatment time (15, 30, 90 and 120 minutes). A treated sample was labelled by the shot type and treatment time: e.g., Alloy 600 treated by stainless steel shots for 15 minutes carried a label of A600ss15 where as that treated by ZrO_2 would be called A600zr15. Using a Buehler diamond tipped saw, cross-sectional segments were cut from the tubing, and further cut into small rectangular coupons. The resulting coupons had an average area of approximately 14 mm^2. The samples were lightly polished with a 0.05 micron alumina pad to remove any oxide film, and the samples were degreased by sonicating in acetone.

2.1 Hardness testing

Samples were prepared by mounting a cross-sectional coupon in a cold epoxy and polishing to a mirror finish, starting with a 500 grit polishing pad and slowly working down to a 0.05 micron alumina pad. A LM 100 Leco Knoop microhardness tester was used to administer the indentations at an applied force of 50 gF. A standard of known hardness was run to ensure adequate calibration before each sample. Starting at the outer diameter of the cross section, three indentations were produced along the length of the outer diameter. The indentations were staggered along the surface in both the x and y directions to prevent interference from the resulting surface deformation of previous measurements.

2.2 Micro-strain Measurements

Small rectangular samples were mounted within a conducting aluminum/carbon epoxy and polished to a mirror finish using the technique described above. These samples were sent to Kinetrics in Toronto for Electron Backscatter diffraction (EBSD) analysis.

2.3 Anodic Polarization Curves

Electrodes were assembled by spot wielding a stainless steel wire to a small sample coupon. These electrodes were lightly polished using 0.05 micron alumina grit, washed with deionized water and sonicated in acetone. The back and sides of the coupon, as well as the wire were coated with a microsheild™ masking aid. A solution of 0.1M $Na_2S_2O_3$ was used for all of the electrochemical experiments, and was made using deionized water with a resistance of 18.2 MΩ. The three electrode cell consisted of a platinum foil counter electrode, a saturated calomel reference electrode (0.2412 V vs SHE), and an A600 working electrode. To purge the system of oxygen, argon gas was vigorously bubbled through for 30 minutes. The flow of argon gas was kept constant throughout the measurements and the cell was maintained at a constant temperature of 25^{o}C. The pH of the solution was slightly below neutral, at approximately 6.5. A reducing potential of -1.2 V was applied for one hour to remove any residual oxide film that may have formed through air exposure. The electrode was maintained at open circuit potential (OCP) for eight hours to allow for stabilization of the current. The polarization curve was run using a Solartron 1286 electrochemical interface potentiostat, at a scan rate of 0.167mV/s. Scanning was initiated at a potential approximately 0.25 V below OCP and terminated at 1.0 V.

2.4 X-ray Photoelectron Spectroscopy (XPS)

Sample electrode preparation was identical to the procedures outlined in the polarization measurements. The samples were electrochemically reduced at -1.2 V for one hour, and held at -0.6, -0.4, -0.2, 0, 0.1, 0.2, 0.4 or 0.6 V for three hours. The samples were washed in deionized water and methanol and stored in de-aerated methanol prior to analysis, which was performed on a Kratos axis ultra XPS instrument. Using an Al kα electron source, high resolution scans were performed on Ni $2p_{3/2}$, Cr $2p_{3/2}$, C 1s, and O 1s at a pass energy of 20 eV. Survey scans were run for each sample using a pass energy of 120 eV. Spectral analysis was completed using CasaXPS™ software.

2.5 Auger Electron Spectroscopy (AES)

Sample preparation and electrochemical treatment was identical to the procedure described above, with the one exception being the electrode storage. All samples were washed in deionized water and methanol before immediate analysis after the electrochemical treatment. To ensure proper conductivity inside the instrument, the masking agent was stripped off of the wire. A PHI 660 SAM instrument was used for analysis at a beam voltage of 5 keV. For each sample, a survey scan was run between 30 and 1030 eV before each depth profile, which analyzed for nickel, chromium, iron, carbon, sulfur and oxygen. The sputter rate was calibrated and determined to be 7.6 nm/min for a mixed NiCr oxide layer.

3. Results

3.1 Microhardness Testing

The hardness testing was performed to provide an indication of how the physical properties of the treated surface had been affected as a result of SMAT. The resulting indentations were converted to Knoop hardness values and plotted as a function of depth, shown in Figure 1. The untreated A600 specimen remained relatively constant, with an average value of 248 HK. The SMAT samples, as expected, displayed higher hardness values, but varied depending on treatment time. Figure 1a shows SMAT samples treated with stainless steel shots and a direct correlation between hardness and treatment time can be made. As the treatment time increases, so does the measured hardness at the surface. Another interesting feature of the plot is the depth at which the maximum Knoop value occurs. While A600ss30 is difficult to see, A600ss120 reaches a maximum close to 100 µm below the surface, whereas A600ss90 peaks immediately below the surface.

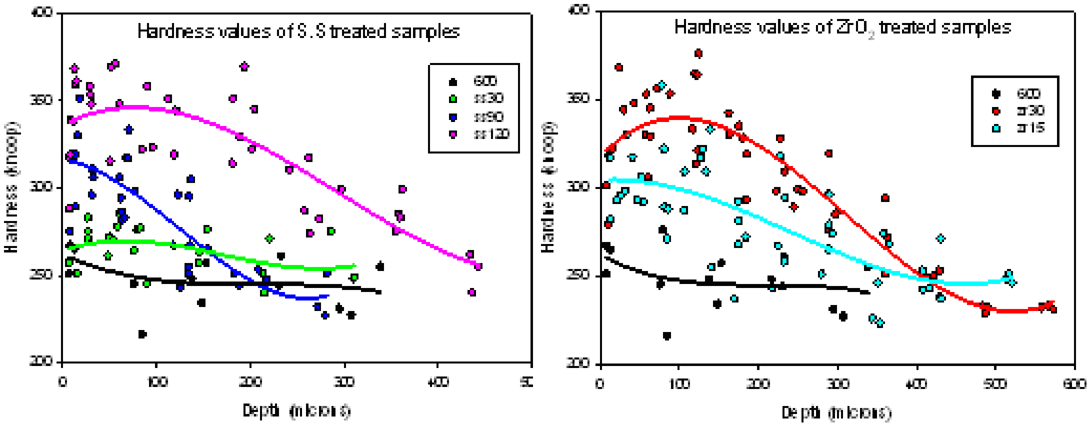

Figure 1 – Hardness plots of a) A600 + stainless steel SMAT samples [A600 (–), A600ss30 (–), A600ss90 (–) A600ss120(–)] and b) A600 + ZrO_2 SMAT samples [A600 (–), A600zr15 (–), A600zr30 (–)]

Figure 1b shows SMAT samples treated with ZrO_2 shots for 15 and 30 minutes. It appears that the ZrO_2 shots were much more efficient at inflicting strain on the sample surface.

For A600zr30, maximum hardness values were very similar to those measured on the stainless steel sample that had been treated for four times longer.

3.2 Anodic Polarization Data

A600, A600zr30, A600zr15 and A600ss120 were analysed using surface and electrochemical techniques. Anodic polarization curves were run on the samples as shown in Figure 2. Plots for all samples demonstrate a modified S-shape curve for a passivating metal. Between -0.6V to -0.4V, the metal undergoes a transition between the active and passive region. Little to no change in current density characterizes the beginning of the passive region, which starts after -0.4V and terminates around 0.6V. At more anodic potentials, the transpassive region is approached.

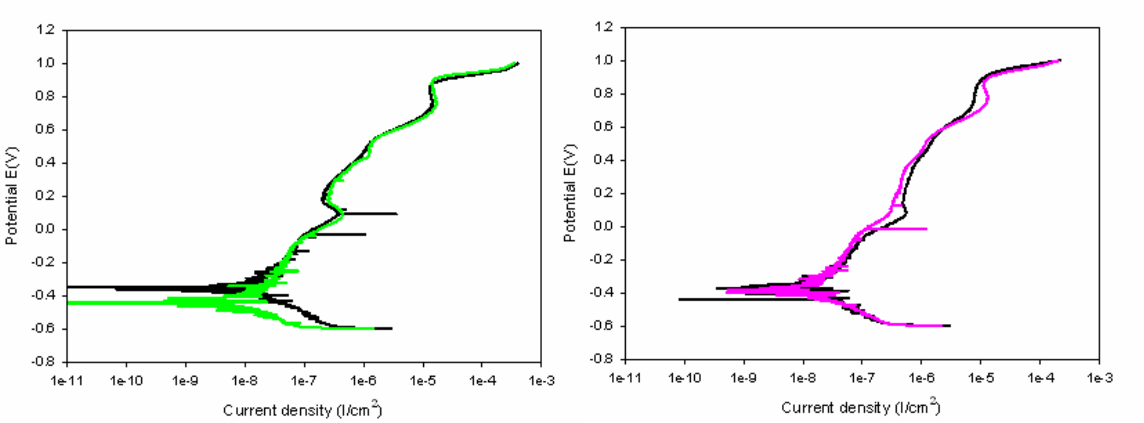

Figure 2 Polarization curves of a) A600 (•) and A600zr15 (•) and b) A600ss120 (•) and A600zr30(•)

Interestingly, the behaviour for A600 and A600zr15 are very similar as indicated by the curve shape, whereas A600ss120 and A600zr30, while slightly different from the previous two, are similar to each other.

3.3 XPS Analysis

The composition of the oxide layer at various potentials was studied using X-ray photoelectron spectroscopy (XPS) and the oxidation states of nickel and chromium were determined.

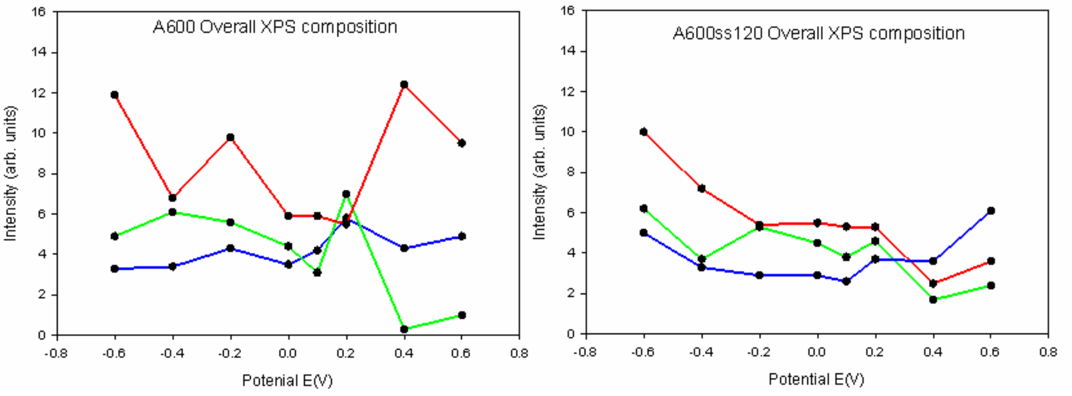

Figure 4 XPS plot of the changes in overall composition of Ni (•), Cr (•), and Fe (•) for a) A600 and b) A600ss120.

For each sample, high resolution scans were performed. On the surface, at least three different chemical forms of chromium were detected: metallic chromium at 573.84 eV, a chromium $Cr(OH)_3$ / CrOOH species at 577.26 eV (+/- 0.12 eV) and a chromium Cr_2O_3 species at 575.63 eV (+/- 0.05 eV). Although only one peak for Cr^{3+} was observed in the spectra, it was resolved that both species were required to make an adequate fit. Similar to chromium, the nickel spectra also suggested the presence of three different species. Nickel metal was detected at 852.54 eV (+/- 0.1 eV), the nickel hydroxide component, $Ni(OH)_2$ at 855.44 eV (+/- 0.2 eV), and NiO at 854.25 eV (+/- 0.2 eV). Unlike chromium, the binding energies for the nickel oxides were slightly higher than values reported in literature (10). Figure 4 shows a plot of the overall compositional values of the film on A600 and A600ss120 at different applied potentials. Within the passive region, significant differences can be observed for nickel, iron and chromium. An in depth analysis on the high resolution spectra was done for these samples, as well as A600zr15 and A600zr30.

3.4 AES Analysis

Auger electron spectroscopy was performed as a means of determining the oxide composition as a function of depth. The thin oxide films formed on the surface at different potentials were sputtered using an Ar^+ beam, and the freshly exposed layers were analysed.

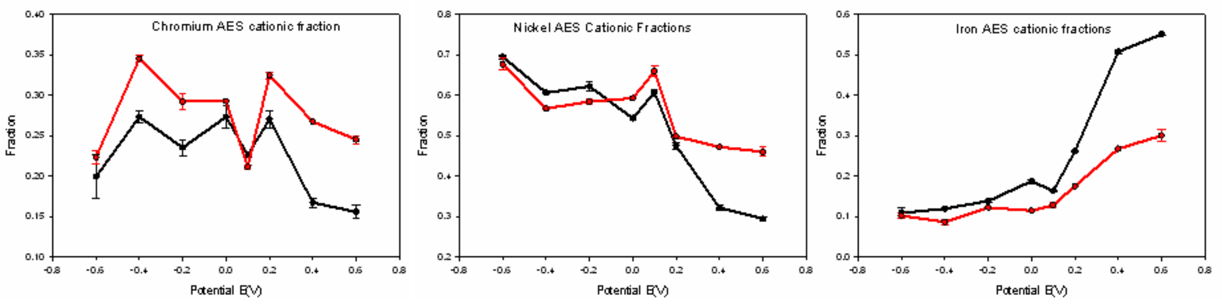

Figure 5 Alloy 600 inner (•) and outer (•) cationic fractions as a function of potential for a) chromium, b) nickel, and c) iron

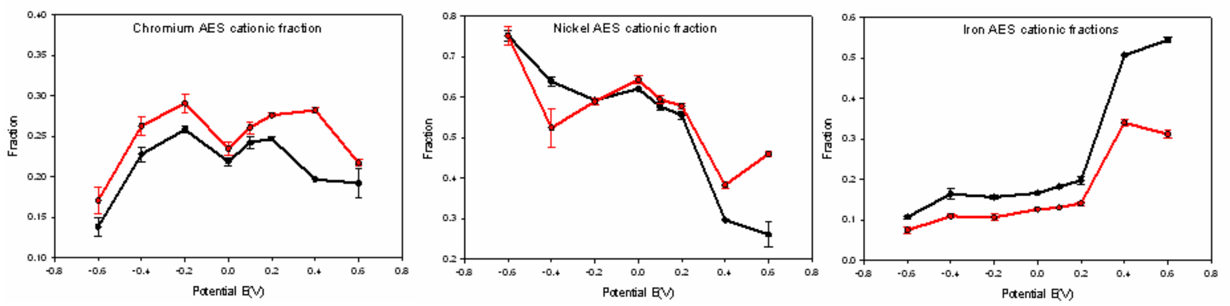

Figure 6 A600ss120 inner (•) and outer (•) cationic fractions at various applied potentials for a) chromium, b) nickel, and c) iron

Figure 5 and 6 reveal the cationic fractions at the various potentials for A600 and A600ss120. A number of observations can be made from these plots. The first is that a bilayer oxide system is present, consisting of a mixed nickel and iron outer layer, and a chromium rich inner layer. Second, the composition of the film is dependant upon the applied potential. In the lower potential range, the majority of the film consists of nickel, while some chromium enrichment is observed. As the potential is increased, the nickel content decreases and the iron content increases.

4 Discussion

Through the repeated application of strain using SMAT, an increase in surface hardness was observed. The extent to which this physical property was altered was largely dependant on the treatment time as well as the shot composition. Increased treatment time directly correlated to an increase in compression strain. The use of a denser material for the shot, such as ZrO_2, meant that each impact on the surface would impart a greater force, thus inducing strain in a more efficient manner. Areas that demonstrated high levels of strain also showed increased hardness values.

4.1 Oxide film formation

As previously mentioned, the oxide formed on the surface of Alloy 600 in 0.1M $Na_2S_2O_3$ was thought to be a bilayer oxide. This structure, as first described by Macdonald, (8, 9), consists of a compact inner barrier layer and a porous outer layer. The formation, growth, and breakdown of this bilayer film can be understood using the point defect model as a reference and the schematic of this model is shown in Figure 7. During film growth, cation vacancies are generated at the barrier/outer layer interface (4) and consumed at the alloy/barrier layer interface (1). At the same time, anion vacancies are formed at the alloy/barrier layer (2) and consumed at the barrier/outer layer (5). Cation vacancies are transported towards the metal (8) and anion vacancies are moved towards the solution (9). Growth of the oxide film occurs in the direction of the metal, and not towards the solution.

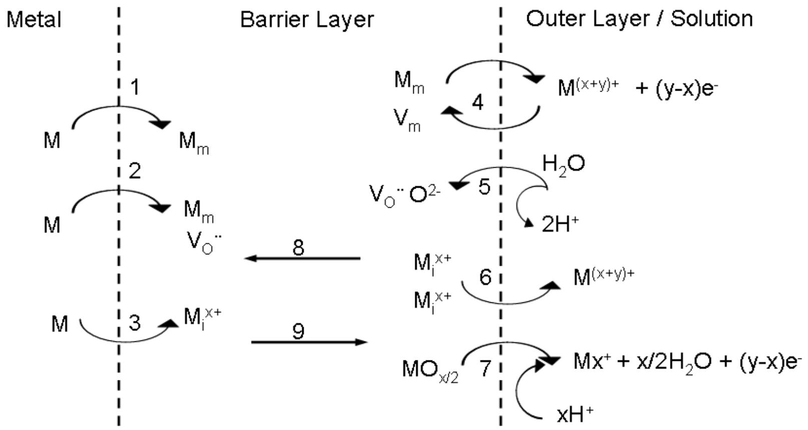

Figure 7 Schematic for the point defect model.

Changes in the oxide composition can be an indicator of changes in film formation. The presence of a larger number of defects may effect the diffusion of ions across the metal, changing the composition of the oxide film.

4.2 Alloy 600

Examining A600, the AES data clearly illustrates changes in the oxide film at various potentials. At lower potentials, nickel is the dominant component of the film, while an iron depletion is also noticed. As the potential becomes more anodic, particularly after 0.2V, the nickel component decreases dramatically, while the iron component increases. Chromium stayed relatively consistent, showing decreased amounts at opposite ends of the potential range. One interesting feature in the chromium plot is the sudden decrease observed at 0.1V. This removal of chromium can be correlated back to the anodic peak observed in the polarization curve. The increase in current density at this potential is due to a loss of chromium from the oxide film.

At lower potentials in the passive region, the composition of the film is dominated by nickel and chromium. At potentials more anodic in the passive region, the composition changes to a film containing much more iron and a lot less nickel. The cationic fraction plots also reveal some clues about the structure of the oxide film. At nearly all measured potentials, chromium was present in the highest concentration in the inner layer, while the opposite behaviour was observed for iron. At potentials lower than 0.2V, the amount of nickel found on the outer surface was similar to the amount found within the oxide film. After 0.2V however, a significant decrease was observed, particularly on the outer surface.

The XPS analysis allowed for the identification of the different nickel and chromium components in the film. Analysis of the high resolution nickel spectra showed that the oxide was mainly composed of nickel hydroxide, with a minimal amount of nickel oxide. The spectra for chromium show that both chromium oxides and hydroxides were both present. For both chromium and nickel, metal peaks were present at all potentials except 0.6V. This indicates that the oxide is a thin film, possibly less than 6 nm based on the inelastic mean free path values for nickel and chromium.

XPS plots showing the overall composition for iron and chromium can be correlated back to the Auger plots relatively well, as the trends observed are very similar. Nickel however, shows an increase in concentration after 0.2V, which does not agree with the Auger depth profile. This may be due a thicker oxide film at higher potentials. Detection limitations become problematic due to the inelastic mean free path of chromium. At potentials of 0.4V and higher, there is very little chromium left on the outer surface. If the outer oxide is too thick, the components of the inner layer will not be measured. The XPS analysis at these potentials will show an excess of nickel as a result.

4.3 SMAT Alloy

The results of the hardness testing showed that there was a direct correlation between induced strain and increased hardness. Whether the altered physical properties had any effect on the corrosion resistance could be interpreted from the chemical and surface analysis. Samples exposed to SMAT for longer periods of time showed an increase in stability in the passive region. Samples A600ss120 and A600zr30 had a reduced anodic peak when compared to A600zr15, which was nearly identical to the untreated sample. When comparing Auger profiling of A600 to A600ss120, differences can be noted, especially for nickel and chromium. For A600ss120, the nickel component in the oxide film remains higher for a larger potential range, while the drop in chromium at the anodic peak potential is not observed. Instead, a slight decrease is noticed at 0V. The XPS data shows little change in iron content when compared to the untreated sample. Chromium is present in higher quantities at the more anodic potentials, although the spike at 0.2V is not observed as it was in A600. The change in the nickel plot was rather curious, as it showed a decrease after 0.2V where A600 showed an increase. Since the Auger plots are similar, this may be a result of a much thinner film forming on the surface.

5 Conclusions

SMAT was found to be an effective treatment in increasing the hardness and strain on a material. Both the treatment time and shot composition were found to be influential processing attributes in SMAT of Alloy 600. The treatment also appeared to increase the corrosion resistance of Alloy 600 at certain potentials. The composition of the oxide films was altered by the surface treatment, possibly by changing the rates of diffusion of nickel and iron, though the extent was largely dependant on treatment parameters.

4. References

[1] G. Sui, J. Titchmarsh, G. Heys, J. Congleton, *Corr. Sci*. **39** (1997) 565

[2] P.A. Page, A. McMinn, *Met. Trans*. **17A** (1986) 877

[3] M. Fontana. Corrosion engineering. McGraw-Hill, Inc. (1986)

[4] R.W. Staehle and J.A. Gorman, *Corrosion* **59** (2003), p. 937 60 (2004) 5; 60 (2004) 115.
R.W. Staehle and J.A. Gorman, *Corrosion* **60** (2004), p. 5.
R.W. Staehle and J.A. Gorman, *Corrosion* **60** (2004), p. 115.

[5] W. Zang, Z. Lu, D. Huang, D. Kong, G. Zhao, J. Congleton, *Corr. Sci*. **43** (2001) 963

[6] K. Lu, J. Lu, *Mat. Sci. eng. A.* **375** (2004) 38

[7] N. Tao, H. Zhang, J. Lu, K. Lu, *Mater. Trans*. **44** (2003) 1919

[8] C.Y. Chao, L.F. Lin, D. Macdonald, *J. electrochem. Soc*. **128** (1981) 1187

[9] L.F. Lin, C.Y. Chao, D. Macdonald, *J. electrochem. Soc*. **128** (1981) 1194

5. Acknowledgements

Funding from CANDU Owners Group (COG) and Ontario Centres of Excellence (OCE) is gratefully acknowledged.